Geochemistry Geophysics Geosystems G3

Article
Volume 11, Number 10
6 October 2010
Q10003, doi:10.1029/2010GC003192
ISSN: 1525-2027

Published by AGU and the Geochemical Society

Plate-driven mantle dynamics and global patterns of mid-ocean ridge bathymetry

Samuel M. Weatherley and Richard F. Katz

Department of Earth Sciences, University of Oxford, South Parks Road, Oxford OX1 3AN, UK (samw@earth.ox.ac.uk)

[1] Global observations of mid-ocean ridge (MOR) bathymetry reveal a correlation between the difference in axial depth across ridge offsets and ridge migration. If upwelling and melt production rates are asymmetric across a ridge axis, three-dimensional (3-D) melt focusing and different crustal thickness across offsets may account for the observed differences in axial depth. In this article we use a 3-D numerical model to constrain the flow and thermal structure of a ridge-transform-ridge plate boundary. By coupling a model of melt focusing to our simulations we generate predictions of crustal thickness and axial depth change across offsets of different lengths. These predictions are consistent with the morphological changes observed along the global MOR system. In making these predictions we produce new constraints on the scale of melt focusing at mid-ocean ridges and on the extent of melt redistribution at the ridge axis. Results from our simulations also suggest that plate-induced mantle dynamics and melt focusing beneath a migrating MOR may produce global, systematic variations in the geochemistry of axial lavas.

Components: 10,200 words, 8 figures, 1 table.

Keywords: mantle; mid-ocean ridge; melt; modeling.

Index Terms: 3035 Marine Geology and Geophysics: Midocean ridge processes; 1032 Geochemistry: Mid-oceanic ridge processes (3614, 8416); 0545 Computational Geophysics: Modeling (1952, 4255).

Received 20 April 2010; **Revised** 2 August 2010; **Accepted** 9 August 2010; **Published** 6 October 2010.

Weatherley, S. M., and R. F. Katz (2010), Plate-driven mantle dynamics and global patterns of mid-ocean ridge bathymetry, *Geochem. Geophys. Geosyst.*, *11*, Q10003, doi:10.1029/2010GC003192.

1. Introduction

[2] Earth's mid-ocean ridges (MORs) are a striking geological feature resulting from plate-mantle interaction. As oceanic plates spread apart, hot asthenospheric mantle upwells and melts adiabatically, supplying the spreading center with material to generate new crust. On a global scale, the physical and petrologic properties of oceanic crust generated at spreading centers are approximately independent of plate kinematics, for fast to slow spreading ridges. These similarities suggest that the fundamental processes governing plate-mantle interaction are uniform throughout the globe. On a regional scale, however, more subtle differences in the physical and chemical properties of oceanic crust become apparent. In this study we use these regional differences to investigate the details of plate-mantle interaction.

[3] Global observations of MOR bathymetry by *Carbotte et al.* [2004] reveal a correlation between the difference in axial depth across ridge offsets and the direction of ridge migration relative to the fixed hot spot reference frame. At the majority of offsets, ridge segments leading with respect to the direction of ridge migration are shallower than trailing segments. The systematic connection between axial depth change across offsets and plate

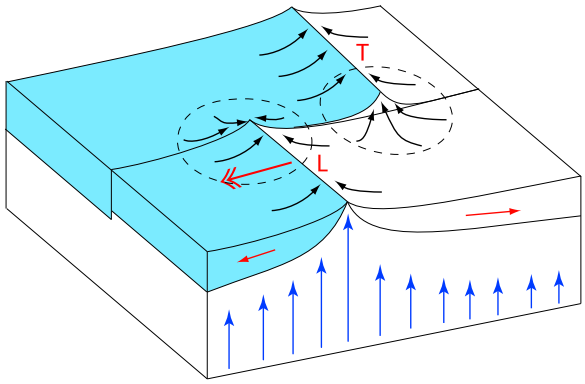

Figure 1. Schematic showing a ridge system consisting of a leading and trailing ridge segment separated by a discontinuity. (The leading and trailing ridge segments are marked L and T, respectively.) Single-headed red arrows show spreading component of plate motion while the double-headed red arrow indicates the direction of ridge migration. The leading plate is colored blue. Blue vertical arrows depict upwelling in the underlying mantle, and black arrows show hypothetical melt focusing trajectories. The dashed circles represent idealized regions of melt focusing, which extend into the mantle beneath the adjacent plates. Melt tapped from these regions contributes to the morphological asymmetry of ridge segments separated by an offset.

kinematics suggests that an explanation might be found in plate motion–induced mantle dynamics. Differences in axial depth across offsets are thought to arise from differences in the volumes of melt being delivered to the leading and trailing ridge segments [*Carbotte et al.*, 2004; *Katz et al.*, 2004]. However, the three-dimensional nature of melt generation and focusing in the vicinity of MOR offsets requires further investigation.

[4] *Carbotte et al.* [2004] suggest that the observed variations in MOR morphology are the result of melt focusing across ridge offsets from a broad, asymmetric zone of upwelling beneath a migrating ridge (Figure 1). Kinematic models of asthenospheric flow beneath a migrating MOR [*Davis and Karsten*, 1986; *Schouten et al.*, 1987] predict faster upwelling and greater melting beneath the leading plate. If the asymmetric melting behavior is captured by melt focusing across offsets, the leading ridge segment is expected to have a thicker crust and shallower axial depth.

[5] Geophysical studies of sub-MOR mantle support the conceptual model of *Carbotte et al.* [2004] and verify the kinematic models of *Davis and Karsten* [1986] and *Schouten et al.* [1987]. Observations of migrating spreading centers show cross-axis asymmetry in mantle properties. Seismic [*Forsyth et al.*, 1998a, 1998b; *Toomey et al.*, 1998] and electrical resistivity [*Evans et al.*, 1999] studies of the MELT region of the East Pacific Rise reveal lower density, lower resistivity, lower seismic velocity, and higher seismic anisotropy beneath the leading plate [*Forsyth et al.*, 1998a]. Subsequent geodynamic models [*Conder et al.*, 2002; *Toomey*, 2002] showed that ridge migration contributes to mantle asymmetry in the MELT region. However, in the MELT region, ridge migration alone does not completely account for the observed magnitude of asymmetry. The authors infer an additional component of asymmetry from hot spots in the nearby Pacific superswell region to completely account for the observed asymmetry. In this respect, the mantle dynamics of the MELT region are a special case. More generally, however, an asymmetric mantle structure is seen beneath migrating MORs across the globe [*Panza et al.*, 2010].

[6] *Katz et al.* [2004] used a 2-D numerical model to simulate asymmetric mantle flow beneath a migrating ridge. These simulations quantified the conceptual model proposed by *Carbotte et al.* [2004]. Figure 2 shows example output from a 2-D simulation after *Katz et al.* [2004]. The mantle flow pattern beneath a migrating MOR is shown in Figure 2a; Figure 2b shows the component of flow induced by ridge migration. To generate predictions of axial depth changes across offsets of different lengths, the authors coupled a simple parametric model of melt focusing to their simulations.

[7] The parametric melt focusing model used by these authors assumes that melt focusing regions are rectangular-shaped in map view and are located at the end of ridge segments. For their experiments, the dimensions of the focusing regions were fixed for all offsets and spreading rates. Melt from these focusing regions was distributed evenly over the first 1 km of the ridge segments, in keeping with the distance over which *Carbotte et al.* [2004] make their observations. Predictions of axial depth asymmetry generated by the 2-D model are consistent with the observations made by *Carbotte et al.* [2004].

[8] Although *Katz et al.* [2004] generate reasonable predictions of axial depth differences across offsets, their model does not consider the fundamentally 3-D nature of transform faults. The mantle flow pattern and thermal structure is two-dimensional and constant along the entire length of each ridge segment. In nature, ridge offsets such as transform faults juxtapose cold, thick lithosphere against warm ridge segments. This temperature difference

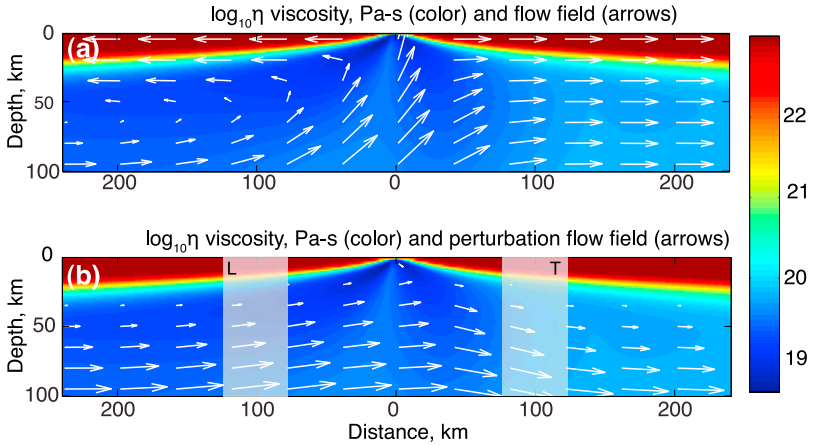

Figure 2. Example output from the 2-D simulations by *Katz et al.* [2004]. (a) The mantle flow pattern beneath a migrating ridge and (b) the component of mantle flow induced by ridge migration are compared. Figure 2a shows a solid mantle flow pattern (white arrows) from 2-D simulation with half spreading rate U_o = 4 cm/yr and ridge migration rate U_r = 4 cm/yr. The ridge is migrating to the left. Colored background shows viscosity in Pa s. Figure 2b shows the component of mantle flow caused by ridge migration. White boxes show the regions within the leading (L) and trailing (T) minor focusing regions.

modifies the thermal structure of the lithosphere and mantle surrounding the offset. Because the thermal structure of the lithosphere and upper mantle close to offsets is three dimensional, mantle flow and melt focusing cannot be fully investigated with a 2-D model. Close to offsets, changes in the temperature structure of the mantle with offset length and spreading rate will affect the shape and dimensions of the focusing regions. Furthermore, at the ridge axis, processes such as melt flow through the porous mantle and cracks are likely to redistribute melt over a substantial section of the ridge axis. These deficiencies of the 2-D simulations can be overcome by extending the model into three spatial dimensions.

[9] In this paper we use 3-D, steady state numerical simulations to investigate the dynamics of the mantle and melt focusing beneath a migrating MOR. We confirm that the magnitude of asymmetry generated solely by ridge migration is sufficient to explain the observations made by *Carbotte et al.* [2004]. However, the behavior of our predictions of axial depth asymmetry across offsets is different to that predicted by the 2-D simulations of *Katz et al.* [2004]. We show that the difference in bathymetry between two adjacent ridge segments depends on the difference in melt volume generated in the focusing regions and the distance over which melt is redistributed at the ridge.

[10] The remainder of this paper is divided into three sections. In section 2 we describe the construction of the numerical model that solves for passively driven, incompressible, creeping mantle flow. Section 2 also details the parameterization of mantle melting, melt focusing, and melt redistribution that we couple to the numerical model. Section 3 shows how predictions of axial depth differences generated by our simulations compare against global MOR data for a range of offsets and spreading rates. In section 4 we discuss how the spreading rate, rate of ridge migration, and geometry of a MOR system influence asthenospheric flow, and to what extent they control differences in axial depth across an offset. Further to this we examine the influence of a viscoplastic rheology on mantle flow and melting beneath a migrating MOR. We also consider how additional geophysical, geochemical, petrological, and numerical studies can better constrain the melt focusing and redistribution processes at MORs.

2. Model Construction

[11] The model is based on a set of coupled partial differential equations to describe incompressible, steady state, passively driven solid mantle flow. We expect that these equations capture the upwelling behavior of mantle beneath migrating MORs. By coupling the computed solid mantle flow field to an existing parameterization of mantle melting [*Katz et al.*, 2003] we determine the melting rate throughout the simulation domain. In the final step of the computation, we apply a model of 3-D melt focusing to the simulations to generate predictions

Table 1. Boundary Conditions[a]

Boundary	Variable	Boundary Condition
$z = 0$	u	$u(x, y, 0) = U_0(x, y)$ where U_0 is the prescribed plate motion
	v	$v = 0$
	w	$w = 0$
	P	BC does not influence the interior of the domain
	T	$T = 0$
$z = Z$	u	$u = U_r$ where U_r is the x component of ridge migration
	v	$v = 0$
	w	$\partial w/\partial z = 0$
	P	$P = 0$
	T	Dimensionless T set equal to dimensionless mantle potential temperature
$x = 0, X$	u	Satisfies discretized form of equation (1)
	v	$v = 0$
	w	$w = 0$
	P	BC does not influence the interior of the domain
	T	$\partial T/\partial x = 0$
$y = 0, Y$	u	No shear stress
	v	No normal stress
	w	No shear stress
	P	BC does not influence the interior of the domain
	T	$\partial T/\partial y = 0$

[a]The domain size is $x \in [0, X]$, $y \in [0, Y]$, $z \in [0, Z]$. The x dimension is parallel to the spreading rate vector, y dimension is parallel to the ridge axes and the z dimension is depth.

of the difference in crustal thickness and axial depth across an offset. Each of these steps is described in more detail below.

2.1. Solid Mantle Flow

[12] The following system of coupled partial differential equations governs passive solid mantle flow.

$$\nabla \cdot \mathbf{v} = 0, \tag{1}$$

$$\nabla P = \nabla \cdot \left[\eta\left(\nabla \mathbf{v} + \nabla \mathbf{v}^T\right)\right], \tag{2}$$

$$\mathbf{v} \cdot \nabla \theta = \kappa \nabla^2 \theta. \tag{3}$$

Here, $\mathbf{v}$ is the three-dimensional mantle velocity, P is dynamic pressure, η is dynamic viscosity, θ is potential temperature, and κ is the thermal diffusivity of mantle rock. Equation (1) is a statement of incompressibility, equation (2) enforces conservation of momentum for an incompressible fluid in the limit of zero Reynolds number and zero buoyancy forces, and equation (3) balances advection and diffusion of heat in steady state.

[13] This system of equations is closed with a constitutive relation for mantle viscosity. The mantle flows by diffusion and dislocation creep; the creep mechanism giving rise to the highest strain rate controls the local viscosity of the mantle. We define the viscosity, η, as

$$\eta = \left(\frac{1}{\eta_{difn}} + \frac{1}{\eta_{disl}}\right)^{-1} \tag{4}$$

where η_{difn} is the viscosity due to pressure- and temperature-dependent diffusion creep and η_{disl} is the viscosity due to pressure-, temperature-, and strain rate–dependent dislocation creep. We combine η_{difn} and η_{disl} in this way to capture transitions in the dominant creep mechanism within the simulation domain. The definitions of η_{difn} and η_{disl} are as follows:

$$\eta_{difn} = A_{difn} \exp\left(\frac{E^*_{difn} + PV^*_{difn}}{RT}\right) \tag{5}$$

$$\eta_{disl} = A_{disl} \exp\left(\frac{E^*_{disl} + PV^*_{disl}}{nRT}\right) \dot{\epsilon}_{II}^{\frac{(1-n)}{n}} \tag{6}$$

where η_{disl} is the viscosity due to pressure- and temperature-dependent diffusion creep, and η_{difn} is the viscosity due to pressure-, temperature-, and strain rate–dependent dislocation creep. A is a proportionality constant, E^* is activation energy, V^* is an activation volume, R is the gas constant, T is temperature, and n is the power law exponent [*Karato and Wu*, 1993; *Hirth and Kohlstedt*, 1996]. $\dot{\epsilon}_{II}$ is the second invariant of the strain rate tensor, providing a measure of the intensity of strain rate.

[14] In our model the lithosphere consists of material with sufficiently high viscosity to be considered rigid. For the purpose of this paper, in each vertical column of grid cells, the base of the lithosphere is defined where $|\partial\eta/\partial z|$ is maximum.

2.2. Boundary Conditions

[15] The governing equations are solved in a reference frame fixed to the migrating ridge. Table 1 summarizes the five boundary conditions for P, T, and $\mathbf{v}$ that are specified on each face of the computational domain.

[16] In a study of current plate motions in the fixed hot spot reference frame, *Small and Danyushevsky* [2003] investigate the global relationship between the half spreading rate U_0 of MORs and the rate of

ridge migration in a direction perpendicular to the ridge axis U_r. They show that the mean ratio of U_r to U_0 is 0.95 with a standard deviation of 0.33. For simplicity, in this study we take U_r to equal U_0. Because the equations are solved in a reference frame fixed to the migrating ridge, the velocity field on the top boundary is set to that of symmetrically spreading plates, and U_r is imposed on the bottom boundary.

[17] The bottom boundary of the domain is intended to correspond to the base of the asthenosphere. For this investigation we take the base of the asthenosphere to be rigid. A large drop in horizontal mantle velocity with increasing depth is expected across the base of the asthenosphere [*Richards et al.*, 2003; *Panza et al.*, 2010]. This indicates that the component of mantle flow induced by ridge migration will be concentrated below the top of the lithosphere-asthenosphere boundary and above the base of the asthenosphere. The radially anisotropic shear velocity structure of sub-MOR mantle may indicate that the depth of the base of the asthenosphere is 200 km [*Nettles and Dziewoński*, 2008]. However, large variations in the thickness of the asthenosphere occur across the globe. For our simulations we use an asthenospheric depth of 300 km. *Katz et al.* [2004] show that the difference in axial depth predicted by the 2-D simulations scales inversely with the asthenospheric thickness.

2.3. Computational Methods

[18] We iteratively solve a finite volume discretization of equations (1)–(3) and the complete set of boundary conditions using a Newton-Krylov solver provided by the Portable, Extensible Toolkit for Scientific Computing (PETSc) [*Balay et al.*, 1997; *Katz et al.*, 2007; *Balay et al.*, 2009]. The dislocation creep term in equation (4) introduces strong nonlinearity into the system, and presents an additional challenge in generating numerical solutions to the governing equations.

[19] To handle the nonlinearity in equation (4) we adopt a continuation method, forcing the variation in viscosity to go from zero to the full predicted variance over a set of iterations of the nonlinear solve [*Knepley et al.*, 2006; *Katz et al.*, 2007]. To smoothly control the variation in viscosity, we set an upper limit of 10^{23} Pa s and use this limit to normalize η to a range between zero and one. The viscosity field η^* used on the m^{th} iteration of the continuation loop is given by

$$\eta^* = \eta^{\alpha_m} \qquad \alpha_m \in [0,1] \tag{7}$$

where $m = 1,2,\ldots, M$. In the first iteration $\alpha_1 = 0$. This yields the solution to the isoviscous case, which is then used as the starting guess for the next step, where $\alpha_2 > \alpha_1$. The continuation loop ends at $\alpha_M = 1$ which corresponds to the full predicted variance in viscosity.

2.4. Melting and Melt Migration

[20] We compute the rate of melt production using a parameterization of mantle melting by *Katz et al.* [2003]. This parameterization expresses melt fraction as a function of pressure, temperature, water content, and modal clinopyroxene. For a given mantle potential temperature, the parameterization predicts that the adiabatic productivity $\mathrm{d}F/\mathrm{d}z|_S$ is approximately constant. The adiabatic melting rate Γ kg/m^3/yr is then calculated as

$$\Gamma = \rho_m W \left.\frac{\mathrm{d}F}{\mathrm{d}z}\right|_S \tag{8}$$

where ρ_m is the density of the mantle, W is the vertical velocity from the solution of equations (1)–(3), and S is entropy. We use equation (8), the solidus of *Katz et al.* [2003], a mantle potential temperature of 1300°C, and an adiabatic productivity of 0.4%/km to calculate the melting rate at each grid cell in the domain. If ridge migration causes any perturbation of W, the melting rate will be asymmetric across the ridge axis.

[21] We assume that the melt from each grid cell percolates vertically through the mantle to the top of the melting region. The upper surface of the melting region is an impermeable boundary that slopes upward toward the ridge axis. Melt migrates uphill along this boundary on streamlines that follow the steepest local slope of the surface, that is

$$\left(\mathbf{i}\frac{\partial h}{\partial x} + \mathbf{j}\frac{\partial h}{\partial y}\right) \times \mathrm{d}\mathbf{s} = 0 \tag{9}$$

where h is the depth to the top of the melting region and ds is an element of arc length along the streamline. This model of melt migration was first proposed by *Sparks and Parmentier* [1991] and has been used in subsequent studies of 3-D melt migration [*Sparks et al.*, 1993; *Magde et al.*, 1997; *Magde and Sparks*, 1997; *Gregg et al.*, 2009]. To determine where along the ridge axis melt is extracted we define a narrow, 2 km wide box, that surrounds the ridge axis and project it onto the top of the melting region. At the point where a streamline crosses into this box, the melt carried

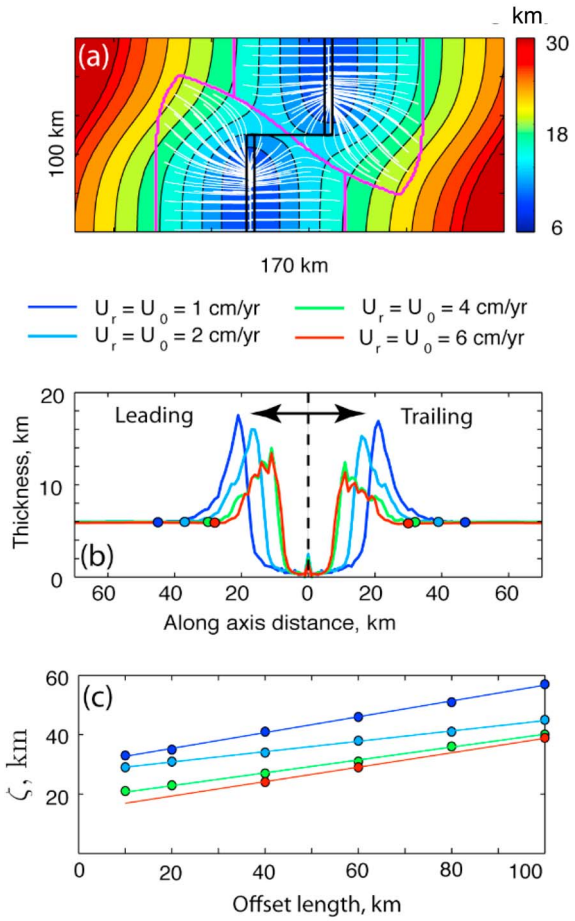

Figure 3. Summary of steps needed to focus melt to the ridge and redistribute it along the ridge axis. (a) Map showing the relationship between solidus depth, focusing region shape and melt focusing trajectories. White streamlines show melt focusing trajectories. Black lines outline the geometry of the ridge system. Magenta lines mark the perimeters of the focusing regions. Colored contours show depth to the top of the melting region. Simulation has U_r = 2 cm/yr and an offset of 40 km. The ridge is migrating to the left. (b) Profiles showing along-axis variation in crustal thickness for simulations with U_r = 1, 2, 4, and 6 cm/yr and an offset of 40 km. Solid dots show the positions at which the gradient of the crustal thickness profiles first departs significantly from zero. The distance between these points and the offset for each simulation is the redistribution distance ζ. (c) Variation in ζ as a function of transform fault length.

along that trajectory is extracted and accumulated at that position on the ridge.

[22] Although melt focusing is thought to be an efficient process, complete extraction of melt from the mantle is unlikely. Petrological studies of abyssal and mantle peridotites [*Warren and Shimizu*, 2010; *Dick et al.*, 2010; *Seyler et al.*, 2001, 2007; *Niu*, 1997], active near-ridge seamounts [*Niu and Batiza*, 1991; *Batiza et al.*, 1990], numerical simulations of mantle dynamics [*Chen*, 1996; *Ghods and Arkani-Hamed*, 2000; *Katz*, 2008], geophysical experiments [*Lizarralde et al.*, 2004], and integration of geophysical and geochemical observations [*Faul*, 2001] all indicate that between 1% and 40% of the melt generated within the melting region is retained in the mantle.

[23] In our models, all of the melt extracted at a ridge segment originates from inside a focusing region. We limit the maximum horizontal extent of the focusing regions from the ridge axis, and hence the fraction of melt extracted at the ridge, by specifying a focusing distance. We assume that the focusing distance increases with spreading rate to maintain a constant crustal thickness of 6 km at an on-axis point 70 km away from the transform fault.

[24] Figure 3a shows predicted melt migration trajectories for a simulation with U_r = 2 cm/yr and an offset of 40 km; colors and contours show the solidus depth. The solidus depth increases close to the transform fault, deflecting melt away from the end of the ridge segment. This leads to on-axis bunching of melt trajectories 10–30 km away from the transform fault.

[25] Along-axis profiles of melt accumulation rate resulting from the melt focusing process described in Figure 3a are shown in Figure 3b. At sufficiently large distances from the transform fault, the crust has a constant thickness of 6 km. Close to the transform fault, deflection of melt trajectories causes large variation in crustal thickness. In nature, such large variations are not seen; for intermediate to fast spreading rates crustal thickness is nearly constant along the length of ridge segments. The constancy of oceanic crustal thickness in nature suggests that along-axis redistribution of melt through cracks and porous mantle works to smooth the initial distribution of melt caused by melt focusing [*Korenaga and Kelemen*, 1997; *Magde et al.*, 2000; *Kelemen et al.*, 2000; *Singh et al.*, 2006a].

[26] In Figure 3b, solid dots indicate the positions at which the gradient of the crustal thickness departs significantly from zero. We assume that the melt between these points and the transform fault is redistributed evenly by along-axis melt transport. Figure 3c shows that the redistribution length ζ, defined by the distance between these points and the transform fault varies linearly with offset length.

2.5. Compensation of Mid-Ocean Ridge Crest Topography

[27] To compare the simulation results against data from the global MOR system we must convert the difference in crustal thickness, computed by the melting and melt migration parameterization, into a difference in axial depth. Spectral studies of MOR topography and gravity suggest that MOR topography is supported by flexure of the oceanic lithosphere [*Cochran*, 1979; *McNutt*, 1979; *Bowin and Milligan*, 1985]. In the flexure model of isostasy the oceanic lithosphere is assumed to behave as a perfectly elastic material. The rigidity of the plate is given by the flexural rigidity, D,

$$D = \frac{ET_e}{12(1-\nu^2)}, \tag{10}$$

where E is Young's modulus, T_e is the elastic thickness of the plate, and ν is Poisson's ratio. In the limit $T_e \rightarrow 0$ the lithosphere has no elastic strength and the flexural model reduces to Airy isostasy. In the limit $T_e \rightarrow \infty$ the plate becomes rigid and does not flex. For dynamic processes, however, T_e approximately corresponds to the depth of the 600°C isotherm [*Watts*, 2007]. The flexure $(t - d)$ generated by periodic loading of an elastic plate is

$$t - d = d\cos(ky)\mathcal{A}\phi_e, \tag{11}$$

where $\mathcal{A}$ is the Airy isostatic response,

$$\mathcal{A} = \frac{\rho_c - \rho_w}{\rho_m - \rho_c}, \tag{12}$$

and ϕ_e is the flexural response function,

$$\phi_e = \left[\frac{Dk^4}{(\rho_m - \rho_c)g} + 1\right]^{-1}. \tag{13}$$

Here, t is the crustal thickness, d is topography, y is the distance along the ridge axis, $k = \pi/\zeta$ is the wave number of the load in the along-ridge direction, and ρ_m, ρ_c, ρ_w are the densities of the mantle, oceanic crust, and seawater, respectively. The flexural response function ϕ_e modifies the Airy isostatic response $\mathcal{A}$ so as to represent flexure.

[28] From equation (11), the difference in axial depth, Δd, between two adjacent ridge segments supported by flexure is related to the difference in crustal thickness, Δt, by

$$\Delta d = \mathcal{C}\Delta t, \tag{14}$$

where

$$\Delta t = \frac{\int_{y_0-\zeta}^{y_0} \gamma_l \, dy - \int_{y_0}^{y_0+\zeta} \gamma_t \, dy}{2\rho_c U_0 \zeta}, \tag{15}$$

the isostatic compensation function $\mathcal{C}$ is

$$\mathcal{C} = [1 + \mathcal{A}\phi_e]^{-1}, \tag{16}$$

y is the direction parallel to the ridge axis, γ_l and γ_t are the mass of melt accumulated per year at the leading and trailing segments of the ridge axis (kg/m/yr), and y_0 is the position of the transform fault. *Watts* [2001] shows that oceanic lithosphere can flexurally support topography over distances of 50 km. Therefore, in applying equation (14) we use a single elastic thickness calculated at a point 50 km off axis on the leading side of the ridge and 50 km away from the fracture zone, and assume E = 100 GPa, $\nu = 0.25$, $g = 9.81$ m/s^2, $\rho_w = 1030$ kg/m^3, $\rho_c = 2900$ kg/m^3, and $\rho_m = 3300$ kg/m^3.

3. Results

[29] Figure 4 shows representative output from a simulation for which the offset is 80 km and U_0 = 4 cm/yr. The grid resolution is 3 km in each direction and, for this simulation only, the base of the asthenosphere is 100 km. Figure 4a shows surfaces of constant upwelling beneath the ridge. Upwelling is uniform in the y direction beneath most of each ridge segment but diminishes within 50 km of the transform fault. There, mantle is drawn across the offset into the region beneath the spreading center. Because the melting rate Γ depends only on the upwelling rate, the vertically integrated melting rate $\int_0^Z \Gamma dz$ gives a more compact perspective of upwelling; it is shown in Figure 4b. In Figure 4, upwelling is fastest, and approximately equal to U_0, at shallow depths immediately beneath the ridge axis. In the region of fastest upwelling our simulations, using experimentally calibrated viscosity laws, predict that the mantle viscosity can be as low as 5×10^{18} Pa s.

[30] The white solid lines in Figure 4b mark the perimeter of the focusing regions. A dashed white line divides each of these focusing regions into a major and minor subregion that are distal and proximal to the transform fault, respectively. Minor subregions terminate at a distance of one redistribution length ζ from the transform fault. If the total melting rate in each of the minor focusing regions

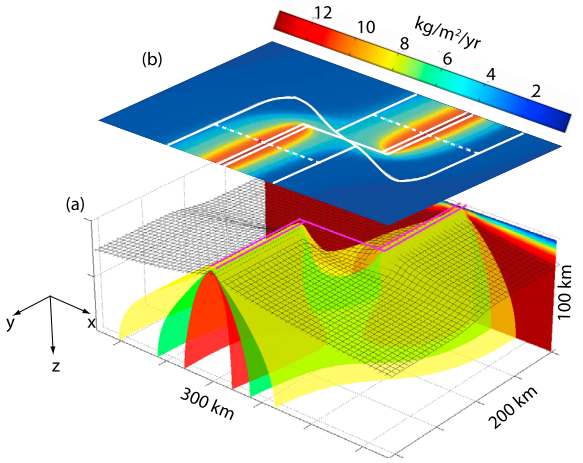

Figure 4. Example output from a 3-D simulation with $U_r = 4$ cm/yr and an offset of 80 km. The ridge is migrating to the left. (a) Three-dimensional image of the upwelling geometry beneath the ridge system. Magenta lines indicate the positions of the transform fault and ridge segments. Red, green, and yellow surfaces show constant upwelling rates of 1, 2, and 2.75 cm/yr, respectively. Upwelling is asymmetric about the ridge axis. Wire mesh marks the base of the lithosphere, defined by the locus of the maximum rate of change in viscosity in the z direction. The back wall shows a 2-D slice through the potential temperature field. Dark red represents the mantle potential temperature (1300°C), and dark blue indicates 0°C. (b) Map of the vertically integrated melting rate, $\int_0^Z \Gamma dz$. White lines show the locations of the ridge segments, transform fault, and the focusing regions. The focusing regions are divided by a white dashed line into major and minor subregions that are distal and proximal to the transform fault, respectively. The vertically integrated melting rate is the melt production rate beneath any point on the surface of the solidus that can be focused to a ridge segment.

is different, then there is a difference in crustal production and $|\Delta d| > 0$. Because the minor focusing regions do not terminate at the transform fault and instead extend some way beyond the ridge axis, they are different to those proposed by *Carbotte et al.* [2004] and *Katz et al.* [2004].

[31] To calculate the behavior of Δd as a function of transform fault length and U_0 when $U_0 = U_r$, we use suites of simulations that maintain constant U_0 and vary offset length. Figure 5 shows predictions of the difference in axial depth Δd generated from four suites of simulations using equation (8). Also shown in Figure 5 are data from the global MOR system [*Carbotte et al.*, 2004] for transform offsets only. These measurements are made by comparing the axial depth of leading and trailing ridge segments. The data are averaged over a 1 km window. Predictions and observations of Δd are for a range of half-spreading rates between 1 and 7 cm/yr and offsets between 0 and 170 km. The focusing distance is 35 km for the suite of simulations with $U_r = 1$ cm/yr, 48 km for the suite with $U_r = 2$ cm/yr,

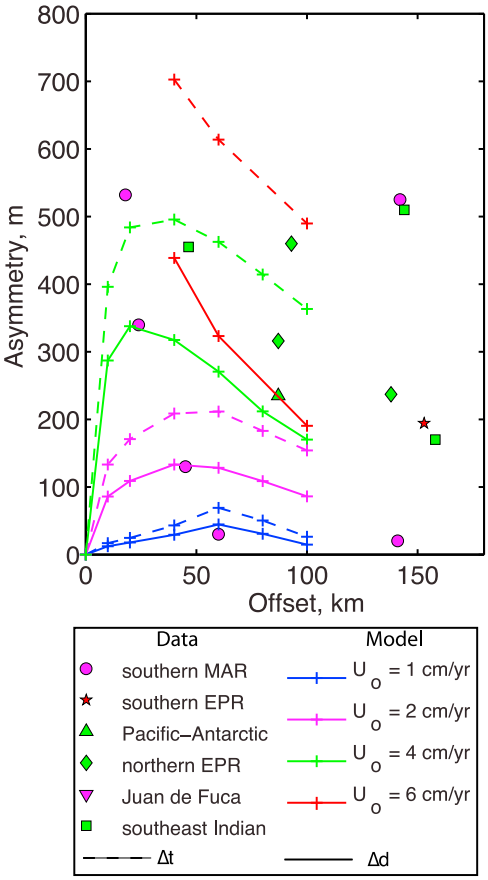

Figure 5. Model results and global data showing the difference in axial depth of two ridge segments separated by an offset, as a function of offset length. All simulations have a grid resolution of 3 km in each direction and an asthenospheric depth of 300 km. Data for transform faults on intermediate and fast spreading ridges (Juan de Fuca, JDF; south East Indian Rise, SEIR; Pacific Antarctic Rise, PACANT; north East Pacific Rise, NEPR; south East Pacific Rise, SEPR) are from *Carbotte et al.* [2004], and data for the southern Mid-Atlantic Ridge (SMAR) are from *Katz et al.* [2004]. The data set covers some 11,000 km of MOR along which 76% of the leading ridge segments have a shallower bathymetry than the trailing ridge segment for all offsets in excess of 5 km. Any data not fitting this trend are excluded. Symbols are colored by the mean half spreading rates. The mean half spreading rates in cm/yr are 1.9 (SMAR), 2.8 (JDF), 3.7 (SEIR), 4.3 (PACANT), 4.6 (NEPR), and 7.0 (SEPR) [*DeMets et al.*, 1994]. Simulations for $U_r = 6$ cm/yr with offsets of 10 km, 20 km, and 80 km did not converge to a solution.

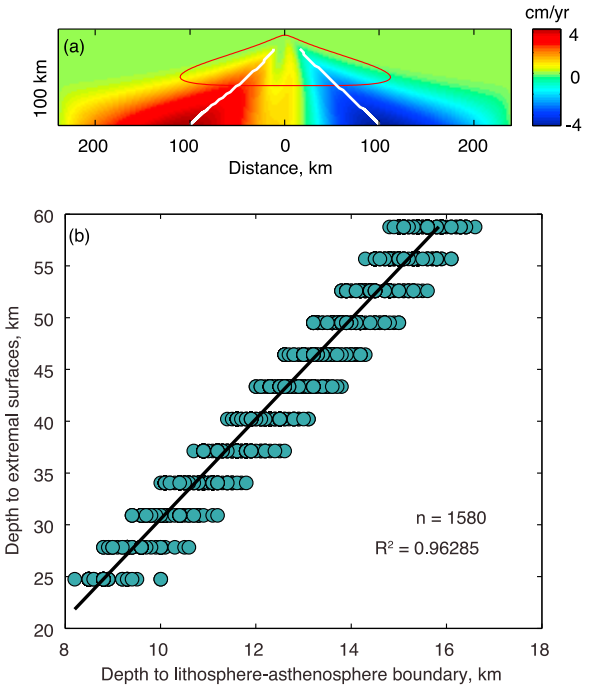

Figure 6. Results from analogous 2-D and 3-D calculations with U_r = 1 cm/yr and an asthenospheric depth of 100 km. (a) For a 2-D simulation, the locations of extremal values of W' and the shape of the melting region. Colored field is the component of upwelling induced by ridge migration, W'. White bold lines mark the extremal values of W' as a function of depth. The red contour outlines the melting region. (b) For the analogous 3-D simulation, the relationship between the depth to the extremal surfaces of W' and the depth to the lithosphere-asthenosphere boundary (LAB). The black line is least squares best fit line taken through all data points.

64 km when U_r = 4 cm/yr, and 73 km when U_r = 6 cm/yr. In each case the focusing distance is less than the width of the melting region, hence peripheral melts are not extracted. We find that the simulations using an asthenospheric thickness of 300 km best fit global ridge data. The amplitude of the difference in crustal thickness predicted by our simulations results scales approximately inversely with the asthenospheric thickness.

[32] For fast spreading rates (U_0 > 4 cm/yr), the model predicts that peak asymmetry in axial depth occurs at offsets of less than 20 km. This distance increases as U_0 decreases. For slow spreading rates (U_0 < 1 cm/yr), Δd reaches a peak at offset lengths greater than 60 km. In general, the MOR data show two broad trends. First, the amplitude of the data increases with spreading rate. Second, the amplitude of the data decreases with increasing offset. The simulations results are consistent with these trends.

4. Discussion

4.1. Three-Dimensional Melt Generation, Focusing, and Redistribution

[33] The simulation results can be understood by considering the component of mantle flow induced by ridge migration. From here onward we refer to this component as the perturbation flow. The vertical component of the perturbation flow W' is of particular importance. As implied by equation (8), the behavior of W' in the minor focusing regions controls the magnitude of the bathymetric asymmetry, Δd.

[34] At sufficiently large distances from the transform fault, the geometry of the lithosphere-asthenosphere boundary (LAB) and behavior of mantle flow is two-dimensional. Here, the LAB curves upward beneath the ridge segments and the perturbation flow has a vertical component of velocity with upwelling on the leading side of the ridge and downwelling on the trailing side. With increasing depth, the loci of maximum $|W'|$ for each horizontal row of grid cells moves away from the ridge along the bold lines shown in Figure 6a. *Katz et al.* [2004] show that the slope of these extremal lines of $|W'|$ varies with spreading rate. This indicates that far from the transform fault, where mantle flow is two-dimensional, the shape of the LAB controls the upwelling behavior of the perturbation flow.

[35] Close to the transform fault the shape of the LAB is three dimensional. Mantle flow in this vicinity has three components of velocity and the control exerted by the LAB on the perturbation flow is not clear. To determine the influence of the LAB on the perturbation flow, we extend the concept of the extremal lines shown in Figure 6a into three dimensions and consider the relationship between the depth to the LAB and the depth to extremal surfaces of $|W'|$. If the LAB controls the perturbation flow, the depth to these extremal surfaces should show a clear relationship to the depth to the LAB.

[36] Figure 6b shows that the depth to the extremal surfaces is correlated with the depth to the LAB. This indicates that the three-dimensional shape of the LAB controls the asymmetric, passive, plate-driven upwelling and melting beneath a migrating MOR system.

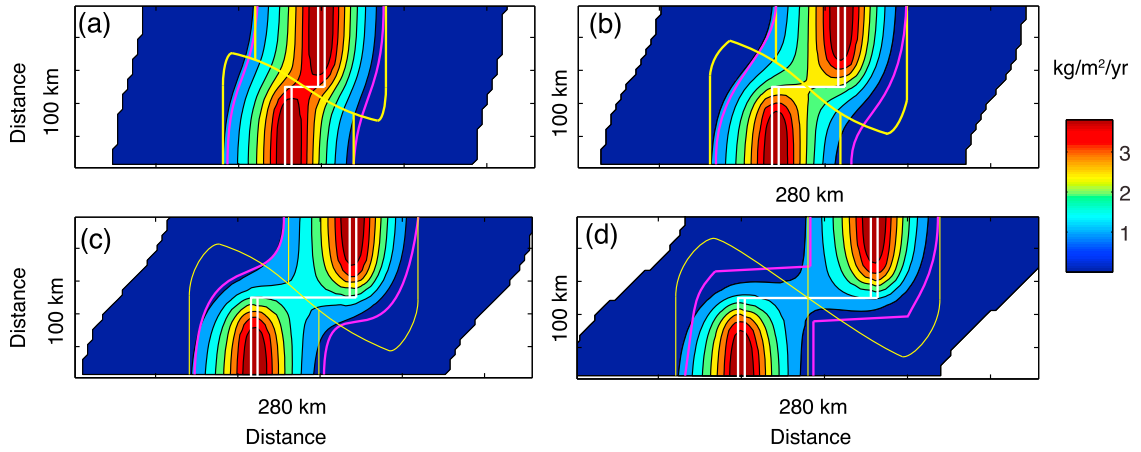

Figure 7. Maps contoured for the melting rate integrated over the depth of the domain. White lines show the trace of the ridge system, yellow lines show the outlines of the focusing regions, and magenta lines show the trace of the extremal surfaces on the base of the melting region. Results taken from simulations with U_r = 1 cm/yr and offsets of (a) 20 km, (b) 40 km, (c) 60 km, and (d) 80 km.

[37] The offset length and spreading rate principally control the shape of the LAB and melting region. Consequently, these two parameters also influence the shape of the focusing regions. Figure 7 shows how the shape of the focusing regions and melting behavior varies for a suite of simulations with U_r = 1 cm/yr and different values of offset. Also shown are the traces of the extremal surfaces where they intersect the bottom of the melting region. The relative spatial positions of the extremal surfaces and minor focusing subregions lends itself to a more detailed explanation of the simulation results.

[38] In the 2-D study by *Katz et al.* [2004], melt is distributed over a constant along-axis distance at the ridge. Consequently, Δd is a maximum when the difference in excess melt production in the focusing regions ΔV is also a maximum. The magnitude of Δd depends on the ratio of ΔV to the volume of space created at the ridge by seafloor spreading. *Katz et al.* [2004] found the offset of maximum excess melt production to be approximately constant at 50 km. For 2-D simulations, the offset of maximum excess melt production corresponds to the offset at which the extremal lines intersect the base of the melting region. In other words, when the excess melt production is a maximum, the minor focusing regions are centered above the locus of largest $|W'|$ within the melting region.

[39] Results from our 3-D simulations (Figure 5) predict that the offset of peak Δt is dependent on spreading rate. Figure 5 shows that the offset of peak Δt decreases with increasing spreading rate. In contrast to *Katz et al.* [2004], the distance over which melt is distributed at the ridge axis, ζ, varies with spreading rate and offset length (Figure 3). The offset of peak Δt, therefore, does not necessarily coincide with the offset of maximum excess melt production but depends on the ratio $\Delta V/\zeta$. When $\Delta V/\zeta$ is greatest, the difference in crustal thickness between two adjacent ridge segments is a maximum. The isostatic compensation function $\mathcal{C}$ given in equation (16) converts Δt into a difference in axial depth, Δd. When $\mathcal{C}V/\zeta$ is greatest, Δd is a maximum. Figure 5 shows that, for a given spreading rate, there is little difference between the offset of peak Δt and peak Δd.

[40] The results in Figure 5 show significant asymmetry about their peak. The component of melting induced by ridge migration is a maximum on the extremal surfaces. It changes most rapidly with horizontal distance on the ridge side of the surfaces. Therefore, ΔV, and thus Δt and Δd, changes most rapidly with offset for offsets less than that of peak Δd.

[41] Figure 5 shows that Δd increases with spreading rate. In plate-driven flow, faster spreading rates drive faster upwelling. In our simulations U_r is equal to U_0, and thus the difference in melt production rate between the two minor focusing regions increases with U_0, causing Δd to increase with U_0.

[42] Although the simulation results shown in Figure 5 describe the general trends of the global MOR data, the data are distributed widely about the simulation results. With such a small number of data points it is difficult to assess how well our

simulations and choice of parameters explain axial depth differences along the global mid-ocean ridge system. Furthermore, local, idiosyncratic, geological processes may induce large scatter in the data.

4.2. Constraining Melt Redistribution Processes

[43] Along mid-ocean ridge systems, melt must be focused from a wide, partially molten region to a narrow zone approximately 5 km wide immediately beneath a ridge segment [*Kelemen et al.*, 2000]. To generate new crust, this melt must be tapped and redistributed on the scale of a ridge segment.

[44] Geophysical observations of the MOR system offer an insight to the physical processes involved in melt redistribution. Seismic studies of fast spreading mid-ocean ridge systems suggest that melt is redistributed in the narrow zone beneath ridge segments to form axial magma chambers [*Collier and Singh*, 1998; *Kent et al.*, 2000; *Nedimovic et al.*, 2005; *Singh et al.*, 2006a, 2006b]. These studies indicate that axial magma chambers for some fast and intermediate spreading rate ridges have a thickness of a few hundred meters and extend nearly continuously along the length of the ridge segment. Seismic reflections [*Singh et al.*, 2006a] from the axial magma chamber beneath the 09°N overlapping spreading center of the East Pacific Rise suggest that melt supply is enhanced beneath the ends of ridge segments. To form such magma chambers, melt must be supplied locally, rather than by large-scale crustal redistribution [*Macdonald et al.*, 1988; *Wang et al.*, 1996]. Field studies suggest that local melt redistribution processes include melt flow through cracks [*Singh et al.*, 2006b], pipe-like features [*Magde et al.*, 2000], and the porous mantle [*Kelemen et al.*, 2000].

[45] Seismic and gravity studies of slow spreading centers show that crustal thickness varies along the length of MOR segments. The amplitude of inferred along-axis variation in crustal thickness decreases with increasing spreading rate [*Lin and Phipps Morgan*, 1992]. For slow spreading ridges, the crust is usually thickest at the center of the segment and thins toward the ends [*Kuo and Forsyth*, 1998; *Lin et al.*, 1990; *Lin and Phipps Morgan*, 1992; *Tolstoy et al.*, 1993; *Detrick et al.*, 1995; *Escartin and Lin*, 1995; *Hooft et al.*, 2000; *Canales et al.*, 2003; *Planert et al.*, 2009]. This feature has been attributed to enhanced melt delivery at segment centers. Figure 3a shows that the shape of the melting region deflects melt away from the end of the ridge segments. The simulations predict that the variation in crustal thickness prior to melt redistribution decreases with increasing spreading rate. This behavior is common to other numerical studies of melt focusing that use the melt migration model of *Sparks and Parmentier* [1991] [*Magde et al.*, 1997; *Magde and Sparks*, 1997; *Gregg et al.*, 2009]. For ridge segments that are tens of kilometers long, this behavior may lead to enhanced melt supply and thicker crust at segment centers. *Bell and Buck* [1992] note that slow spreading ridges with thick crust do not show large crustal thickness variation on a segment scale, suggesting that melt redistribution may be a function of crustal thermal structure.

[46] Although geophysical investigations can constrain melt redistribution processes on a large scale, the scale and extent of these processes may be studied more intimately using geochemical and petrological techniques. Geochemical variations in ridge axis lavas can yield information about the source region and geological history of the parent magma. Petrological mapping of oceanic basalts at MORs indicates that igneous rocks formed close to ridge offsets have a deeper source region and lower extent of melting than those elsewhere along the ridge segment [*Langmuir and Bender*, 1984; *Langmuir et al.*, 1986; *Reynolds and Langmuir*, 1997]. In samples taken along the axis of the north East Pacific Rise, the most enriched geochemical signals are found consistently at the ends of leading ridge segments [*Carbotte et al.*, 2004]. These excursions peak very close to the offset and typically decay rapidly with distance along the ridge axis.

[47] Our simulations suggest that geochemical variations can exist between the melt focused from the leading and trailing focusing regions. Unless the direction of ridge migration is parallel to the ridge trace, the leading focusing region samples relatively deep mantle in advance of the trailing focusing region. Consequently, melts produced in the leading minor melt focusing region will be among the most enriched and compositionally diverse. In contrast, because the trailing minor focusing region lies in the wake of the leading ridge segment, melt generated in this trailing subregion will have smaller variations in trace element geochemistry. The amplitude of these variations will be greatest when the direction of ridge migration is perpendicular to the ridge axis. The amplitude will decrease with the angle between the direction of ridge migration and the ridge axis. Hence our model is compatible with the geo-

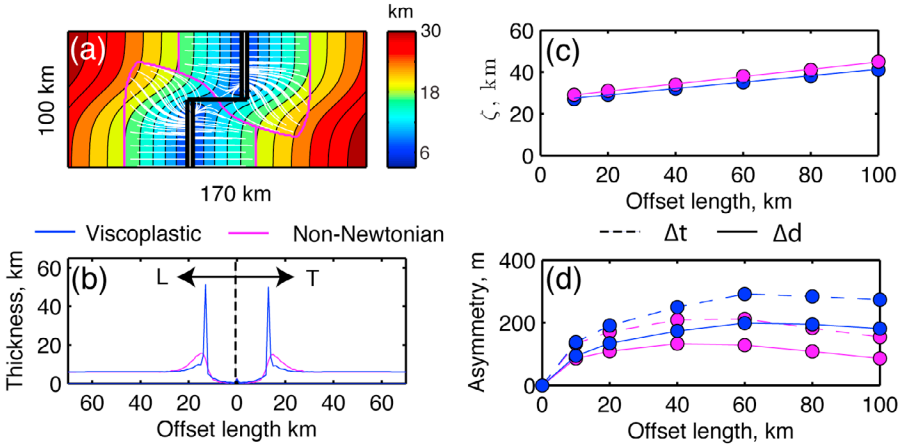

Figure 8. Comparison of results from two suites of simulations, one having a non-Newtonian rheology (magenta lines) and the other using a viscoplastic rheology (blue lines). All simulations have $U_r = 2$ cm/yr and a domain depth of 300 km. (a) Map showing the relationship between solidus depth, focusing region shape, and melt focusing trajectories. White streamlines show melt focusing trajectories. Black lines outline the geometry of the ridge system. Magenta lines mark the perimeters of the focusing regions. Colored contours show depth to the top of the melting region. The transform fault length is 40 km. Ridge is migrating to the left. Figure 8a be compared directly with its non-Newtonian analogue in Figure 3a. (b) Profiles showing the along-axis crustal thickness prior to redistribution of the melt. The offset length for these simulations is 40 km. L and T denote the leading and trailing ridge segments, respectively. (c) Variation in the redistribution length ζ as a function of transform fault length. (d) Comparison of the difference in crustal thickness (Δt, dashed) and axial depth (Δd, solid) for the two suites of simulations as a function of offset length.

chemical observations made by *Carbotte et al.* [2004].

4.3. Mantle Rheology

[48] Predictions of mantle dynamics and thermal structure generated by our simulations depend largely on the assumed mantle rheology. For this study we assume that the mantle is a non-Newtonian fluid that deforms by combined diffusion and dislocation creep. *Katz et al.* [2004] show that this choice of rheology improves the fit between simulation results and global MOR data over diffusion creep alone. Other numerical experiments of mantle flow near transform faults by *Behn et al.* [2007] and *Gregg et al.* [2009] explore the importance of using a viscoplastic rheology. They show that simulations with a viscoplastic rheology, over those with a constant or temperature-dependent viscosity, better fit geophysical and geochemical observables.

[49] Figure 3 demonstrates the importance of the mantle thermal structure to melt focusing. The experiments by *Behn et al.* [2007] and *Gregg et al.* [2009] predict that a viscoplastic rheology tends to localize deformation around the ridge segments and transform faults. This causes the mantle around the transform fault to be warmer and reduces the along-axis distance over which melt is focused away from the offset.

[50] To examine the influence of a viscoplastic rheology on our simulations we define a viscoplastic rheology:

$$\eta = \left(\frac{1}{\eta_{difn}} + \frac{1}{\eta_{disl}} + \frac{1}{\eta_{bsa}}\right)^{-1}, \tag{17}$$

where η_{bsa} is a brittle strength approximation using Byerlee's law. The viscosity associated with brittle failure η_{bsa} is given by [*Chen and Morgan*, 1990]

$$\eta_{bsa} = \frac{\tau}{\sqrt{2}\dot{\epsilon}_{II}}, \tag{18}$$

in which brittle strength is approximated by a friction law:

$$\tau = \mu\rho g z + c_0. \tag{19}$$

Here, μ is the frictional coefficient (0.6), g is the acceleration due to gravity, and c_0 is the cohesion (10 MPa).

[51] Figure 8 compares two identical suites of simulations with U_r = 2 cm/yr, except that one (shown in pink) uses the non-Newtonian viscosity defined in equation (4), and the other (shown in blue) assumes the viscoplastic rheology given in

equation (17). For the viscoplastic simulations, the focusing distance is 48 km. This returns a crustal thickness of 6 km at an on-axis point 70 km from the transform fault. Comparison of Figure 8a with Figure 3a demonstrates that the of the morphology of the melting region differs between analogous simulations. The viscoplastic rheology enhances the upwelling and thermal regime around the ridge segments and transform fault. This increases the amount of melt focused across offsets and, around the transform fault, decreases the depth to the melting region.

[52] Figures 8a and 8b show that the change in morphology of the melting region alters the delivery of melt to the ridge axis. In the case of a viscoplastic rheology melt is delivered to a point close to the transform fault. However, Figures 8b and 8c show that the neither the position of maximum melt delivery, or the redistribution distance ζ are changed much.

[53] Figure 8d shows the effect of a viscoplastic rheology on axial depth differences for a range of transform fault lengths. The dashed curves show the difference in crustal thickness as a function of offset length. Assuming flexural support of ridge topography, these are converted into a difference in axial depth. For all nonzero offsets viscoplastic simulations predict greater asymmetry in crustal thickness and axial depth. This difference in asymmetry arises because the viscoplastic rheology increases the amount of melt focused across offsets (Figures 8a and 3a). The significance of this effect increases with offset, resulting in increasingly greater differences in predicted crustal thickness and axial depth.

5. Conclusion

[54] By extending the 2-D model of asthenospheric flow and melting by *Katz et al.* [2004] into three dimensions, we confirm that plate-induced mantle dynamics can account for morphological changes observed along the global MOR system. Our model assumes that the mantle viscosity is high enough for asthenospheric flow to be effectively plate driven. Ridge migration perturbs asthenospheric flow, causing faster upwelling and enhanced melting beneath the plate that is leading with respect to the direction of ridge migration in the hot spot reference frame. Under reasonable assumptions of 3-D melt focusing, this melting asymmetry causes a difference in axial depth and crustal thickness of ridge segments separated by an offset. The sense of mantle asymmetry predicted by our model is consistent with that seen in geophysical observations of MORs [*Forsyth et al.*, 1998a; *Panza et al.*, 2010]. Predictions of differences in axial depth across ridge offsets generated by our models describe the general trend and amplitude of global MOR data. The amplitude of the data can be fit with a widely used model of 3-D melt focusing [*Sparks and Parmentier*, 1991] and an asthenospheric thickness of 300 km. To smooth variations in crustal thickness close to transform faults, we assume that melt is redistributed along the ridge segment axis by melt flow through the porous mantle and cracks. Additional experiments that include a viscoplastic rheology predict enhanced mantle temperatures and upwelling rates around the ridge segments and transform fault. This leads to an increase in the predicted asymmetry in axial depth. Future models can further constrain shallow mantle and lithospheric processes that distribute melt at the ridge axis by using a parameterization of mantle melting and incompatible element behavior.

Acknowledgments

[55] The authors thank A. B. Watts for useful discussions and S. M. Carbotte for discussions and provision of MOR data. We thank M. Behn and R. Buck for careful and helpful reviews that improved this manuscript. Oxford Supercomputing Centre provided supercomputing time and technical support. S.M.W. is supported by a UK Natural Environment Research Council Research Studentship. R.F.K. is a Research Councils UK Academic Fellow.

References

Balay, S., W. D. Gropp, L. Curfman McInnes, and B. F. Smith (1997), Efficient management of parallelism in object oriented numerical software libraries, in *Modern Software Tools in Scientific Computing*, edited by E. Arge, A. M. Bruaset, and H. P. Langtangen, pp. 163–202, Birkhäuser, Boston.

Balay, S., K. Buschelman, V. Eijkhout, W. D. Gropp, D. Kaushik, M. G. Knepley, L. Curfman McInnes, B. F. Smith, and H. Zhang (2009), PETSc users manual, *Rep. ANL-95/11*, rev. 3.0.0, Argonne Natl. Lab., Argonne, Ill. (Available at http://www.mcs.anl.gov/petsc/petsc-as/)

Batiza, R., Y. L. Niu, and W. C. Zayac (1990), Chemistry of seamounts near the East Pacific Rise—Implications for the geometry of subaxial mantle flow, *Geology*, *18*(11), 1122–1125.

Behn, M., M. S. Boettcher, and G. Hirth (2007), Thermal structure of oceanic transform faults, *Geology*, *35*(4), 307–310.

Bell, R. E., and W. R. Buck (1992), Crustal control of ridge segmentation inferred from observations of the Reykjanes Ridge, *Nature*, *357*, 583–586.

Bowin, C., and J. Milligan (1985), Negative gravity-anomaly over spreading rift valleys—Mid-Atlantic Ridge at 26°N, *Tectonophysics*, *113*(3–4), 233–256.

Canales, J. P., R. S. Detrick, D. R. Toomey, and W. S. D. Wilcock (2003), Segment-scale variations in the crustal structure of 150–300 kyr old fast spreading oceanic crust (East Pacific Rise, 8° 15′N–10° 5′N) from wide-angle seismic refraction profiles, *Geophys. J. Int.*, *152*(3), 766–794.

Carbotte, S. M., C. Small, and K. Donnelly (2004), The influence of ridge migration on the magmatic segmentation of mid-ocean ridges, *Nature*, *429*(6993), 743–746.

Chen, Y. J. (1996), Constraints on melt production rate beneath the mid-ocean ridges based on passive flow models, *Pure Appl. Geophys.*, *146*(3–4), 589–620.

Chen, Y., and W. J. Morgan (1990), A nonlinear rheology model for mid-ocean ridge axis topography, *J. Geophys. Res.*, *95*, 17,583–17,604.

Cochran, J. R. (1979), Analysis of isostasy in the world's oceans: 2. Midocean ridge crests, *J. Geophys. Res.*, *84*(B9), 4713–4729.

Collier, J., and S. Singh (1998), A seismic inversion study of the axial magma chamber reflector beneath the East Pacific Rise near 10°N, *Geol. Soc. London Spec. Publ.*, *148*(1), 17–28.

Conder, J. A., D. W. Forsyth, and E. M. Parmentier (2002), Asthenospheric flow and asymmetry of the East Pacific Rise, MELT area, *J. Geophys. Res.*, *107*(B12), 2344, doi:10.1029/2001JB000807.

Davis, E. E., and J. L. Karsten (1986), On the cause of the asymmetric distribution of seamounts about the Juan de Fuca ridge: Ridge-crest migration over a heterogeneous asthenosphere, *Earth Planet. Sci. Lett.*, *79*(3–4), 385–396.

DeMets, C., R. G. Gordon, D. F. Argus, and S. Stein (1994), Effect of recent revisions to the geomagnetic reversal timescale on estimates of current plate motions, *Geophys. Res. Lett.*, *21*(20), 2191–2194.

Detrick, R. S., H. D. Needham, and V. Renard (1995), Gravity anomalies and crustal thickness variations along the Mid-Atlantic ridge between 33°N and 40°N, *J. Geophys. Res.*, *100*(B3), 3767–3787.

Dick, H., C. Lissenberg, and J. Warren (2010), Mantle melting, melt transport, and delivery beneath a slow-spreading ridge: The Paleo-MAR from 23°15′N to 23°45′N, *J. Petrol.*, *51*(1–2), 425–467.

Escartin, J., and J. A. Lin (1995), Ridge offsets, normal faulting, and gravity-anomalies of slow-spreading ridges, *J. Geophys. Res.*, *100*(B4), 6163–6177.

Evans, R. L., et al. (1999), Asymmetric electrical structure in the mantle beneath the East Pacific Rise at 17 °S, *Science*, *286*(5440), 752–756.

Faul, U. H. (2001), Melt retention and segregation beneath mid-ocean ridges, *Nature*, *410*(6831), 920–923.

Forsyth, D. W., et al. (1998a), Imaging the deep seismic structure beneath a mid-ocean ridge: The MELT Experiment, *Science*, *280*(5367), 1215–1218.

Forsyth, D. W., S. C. Webb, L. M. Dorman, and Y. Shen (1998b), Phase velocities of Rayleigh waves in the MELT experiment on the East Pacific Rise, *Science*, *280*(5367), 1235–1238.

Ghods, A., and J. Arkani-Hamed (2000), Melt migration beneath mid-ocean ridges, *Geophys. J. Int.*, *140*(3), 687–697.

Gregg, P. M., M. D. Behn, J. Lin, and T. L. Grove (2009), Melt generation, crystallization, and extraction beneath segmented oceanic transform faults, *J. Geophys. Res.*, *114*, B11102, doi:10.1029/2008JB006100.

Hirth, G., and D. Kohlstedt (1996), Water in the oceanic upper mantle: Implications for rheology, melt extraction and the evolution of the lithosphere, *Earth Planet. Sci. Lett.*, *144* (1–2) 93–108.

Hooft, E. E. E., R. S. Detrick, D. R. Toomey, J. A. Collins, and J. Lin (2000), Crustal thickness and structure along three contrasting spreading segments of the Mid-Atlantic Ridge, 33.5°–35°N, *J. Geophys. Res.*, *105*(B4), 8205–8226.

Karato, S., and P. Wu (1993), Rheology of the upper mantle: A synthesis, *Science*, *260*(5109), 771–778.

Katz, R. (2008), Magma dynamics with the enthalpy method: Benchmark solutions and magmatic focusing at mid-ocean ridges, *J. Petrol.*, *49*(12), 2099–2121.

Katz, R. F., M. Spiegelman, and C. H. Langmuir (2003), A new parameterization of hydrous mantle melting, *Geochem. Geophys. Geosyst.*, *4*(9), 1073, doi:10.1029/2002GC000433.

Katz, R. F., M. Spiegelman, and S. M. Carbotte (2004), Ridge migration, asthenospheric flow and the origin of magmatic segmentation in the global mid-ocean ridge system, *Geophys. Res. Lett.*, *31*, L15605, doi:10.1029/2004GL020388.

Katz, R., M. Knepley, B. Smith, M. Spiegelman, and E. Coon (2007), Numerical simulation of geodynamic processes with the Portable Extensible Toolkit for Scientific Computation, *Phys. Earth Planet. Inter.*, *163*(1–4), 52–68.

Kelemen, P. B., M. Braun, and G. Hirth (2000), Spatial distribution of melt conduits in the mantle beneath oceanic spreading ridges: Observations from the Ingalls and Oman ophiolites, *Geochem. Geophys. Geosyst.*, *1*(7), 1005, doi:10.1029/1999GC000012.

Kent, G. M., et al. (2000), Evidence from three-dimensional seismic reflectivity images for enhanced melt supply beneath mid-ocean ridge discontinuities, *Nature*, *406*(6796), 614–618.

Knepley, M. G., R. F. Katz, and B. F. Smith (2006), Developing a geodynamics simulator with PETSc, in *Numerical Solution of Partial Differential Equations on Parallel Computers*, *Lect. Notes in Comput. Sci. and Eng.*, vol. 51, edited by A. M. Bruaset and A. Tveito, pp. 413–438, Springer, Berlin.

Korenaga, J., and P. B. Kelemen (1997), Origin of gabbro sills in the Moho transition zone of the Oman ophiolite: Implications for magma transport in the oceanic lower crust, *J. Geophys. Res.*, *102*(B12), 27,729–27,749.

Kuo, B. Y., and D. W. Forsyth (1998), Gravity anomalies of the ridge-transform system in the South Atlantic between 31°S and 34.5°S—Upwelling centres and variations in crustal thickness, *Mar. Geophys. Res.*, *10*(3–4), 205–232.

Langmuir, C. H., and J. F. Bender (1984), The geochemistry of oceanic basalts in the vicinity of transform faults—Observations and implications, *Earth Planet. Sci. Lett.*, *69*(1), 107–127.

Langmuir, C. H., J. F. Bender, and R. Batiza (1986), Petrological and tectonic segmentation of the East Pacific Rise, 5° 30′–14° 30′N, *Nature*, *322*(6078), 422–429.

Lin, J., and J. Phipps Morgan (1992), The spreading rate dependence of three-dimensional mid-ocean ridge gravity structure, *Geophys. Res. Lett.*, *19*(1), 13–16.

Lin, J., G. M. Purdy, H. Schouten, J. C. Sempere, and C. Zervas (1990), Evidence from gravity data for focused magmatic accretion along the Mid-Atlantic ridge, *Nature*, *344*(6267), 627–632.

Lizarralde, D., J. B. Gaherty, J. A. Collins, G. Hirth, and S. D. Kim (2004), Spreading-rate dependence of melt extraction at

mid-ocean ridges from mantle seismic refraction data, *Nature*, *432*, 744–747.

Macdonald, K. C., P. J. Fox, L. J. Perram, M. F. Eisen, R. M. Haymon, S. P. Miller, S. M. Carbotte, M. H. Cormier, and A. N. Shor (1988), A new view of the mid-ocean ridge from the behaviour of ridge-axis discontinuities, *Nature*, *335*(6187), 217–225.

Magde, L. S., and D. W. Sparks (1997), Three-dimensional mantle upwelling, melt generation, and melt migration beneath segment slow spreading ridges, *J. Geophys. Res.*, *102*(B9), 20,571–20,583.

Magde, L., D. Sparks, and R. Detrick (1997), The relationship between buoyant mantle flow, melt migration, and gravity bull's eyes at the Mid-Atlantic Ridge between 33°N and 35°N, *Earth Planet. Sci. Lett.*, *148*(1–2), 59–67.

Magde, L., A. Barclay, D. Toomey, R. Detrick, and J. Collins (2000), Crustal magma plumbing within a segment of the Mid-Atlantic Ridge, 35°N, *Earth Planet. Sci. Lett.*, *175*(1–2), 55–67.

McNutt, M. K. (1979), Compensation of oceanic topography: An application of the response function technique to the Surveyor area, *J. Geophys. Res.*, *84*, 7589–7598.

Nedimovic, M. R., S. M. Carbotte, and A. J. Harding (2005), Frozen magma lenses below the oceanic crust, *Nature*, *436*(25), 1149–1152.

Nettles, M., and A. M. Dziewoński (2008), Radially anisotropic shear velocity structure of the upper mantle globally and beneath North America, *J. Geophys. Res.*, *113*, B02303, doi:10.1029/2006JB004819.

Niu, Y. (1997), Mantle melting and melt extraction processes beneath ocean ridges: Evidence from abyssal peridotites, *J. Petrol.*, *38*(8), 1047–1074.

Niu, Y. L., and R. Batiza (1991), An empirical-method for calculating melt compositions produced beneath midocean ridges: Application for axis and off-axis (seamounts) melting, *J. Geophys. Res.*, *96*(B13), 21,753–21,777.

Panza, G., C. Doglioni, and A. Levshin (2010), Asymmetric ocean basins, *Geology*, *38*(1), 59–62.

Planert, L., E. R. Flueh, and T. J. Reston (2009), Along- and across-axis variations in crustal thickness and structure at the Mid-Atlantic Ridge at 5°S obtained from wide-angle seismic tomography: Implications for ridge segmentation, *J. Geophys. Res.*, *114*, B09102, doi:10.1029/2008JB006103.

Reynolds, J. R., and C. H. Langmuir (1997), Petrological systematics of the Mid-Atlantic Ridge south of Kane: Implications for ocean crust formation, *J. Geophys. Res.*, *102*(B7), 14,915–14,946.

Richards, M., S. Morris, F. Busse, and A. Lenardic (2003), Towards a physical understanding of the effects of depth-dependent rheology on mantle convection, *Eos Trans. AGU*, *84*(46), Fall Meet. Suppl., Abstract S11G-06.

Schouten, H., H. J. B. Dick, and K. D. Klitgord (1987), Migration of mid-ocean-ridge volcanic segments, *Nature*, *326*(6116), 835–839.

Seyler, M., M. J. Toplis, J.-P. Lorand, A. Luget, and M. Cannat (2001), Clinopyroxene microtextures reveal incompletely extracted melts in abyssal peridotites, *Geology*, *29*(2), 155–158.

Seyler, M., J. P. Lorand, H. J. B Dick, and M. Drouin (2007), Pervasive melt percolation reactions in ultra-depleted refractory harzburgites at the Mid-Atlantic Ridge, 15° 20′N: ODP Hole 1274A, *Contrib. Mineral. Petrol.*, *153*(3), 303–319.

Singh, S. C., et al. (2006a), Seismic reflection images of the Moho underlying melt sills at the East Pacific Rise, *Nature*, *442*(7100), 287–290.

Singh, S. C., W. C. Crawford, H. Carton, T. Seher, V. Combier, M. Cannat, J. P. Canales, D. Düsünür, J. Escartin, and J. M. Miranda (2006b), Discovery of a magma chamber and faults beneath a Mid-Atlantic Ridge hydrothermal field, *Nature*, *442*(7106), 1029–1032.

Small, C., and L. Danyushevsky (2003), Plate-kinematic explanation for mid-oceanic-ridge depth discontinuities, *Geology*, *31*(5), 399–402.

Sparks, D., and E. Parmentier (1991), Melt extraction from the mantle beneath spreading centers, *Earth Planet. Sci. Lett.*, *105*(4), 368–377.

Sparks, D. W., E. M. Parmentier, and J. Phipps Morgan (1993), Three-dimensional mantle convection beneath a segmented spreading center: Implications for along-axis variations in crustal thickness and gravity, *J. Geophys. Res.*, *98*(B12), 21,977–21,995.

Tolstoy, M., A. J. Harding, and J. A. Orcutt (1993), Crustal thickness on the Mid-Atlantic Ridge—Bulls-eye gravity-anomalies and focused accretion, *Science*, *262*(5134), 726–729.

Toomey, D. (2002), Asymmetric mantle dynamics in the MELT region of the East Pacific Rise, *Earth Planet. Sci. Lett.*, *200*(3–4), 287–295.

Toomey, D. R., W. S. D. Wilcock, S. C. Solomon, W. C. Hammond, and J. A. Orcutt (1998), Mantle seismic structure beneath the MELT region of the East Pacific Rise from P and S wave tomography, *Science*, *280*(5367), 1224–1227.

Wang, X., J. R. Cochran, and G. A. Barth (1996), Gravity anomalies, crustal thickness, and the pattern of mantle flow at the fast spreading East Pacific Rise, 9°–10°N: Evidence for three-dimensional upwelling, *J. Geophys. Res.*, *101*(B8), 17,927–17,940.

Warren, J., and N. Shimizu (2010), Cryptic variations in abyssal peridotite compositions: Evidence for shallow-level melt infiltration in the oceanic lithosphere, *J. Petrol.*, *51*(1–2), 1–29.

Watts, A. B. (2001), *Isostasy and Flexure of the Lithosphere*, Cambridge Univ. Press, Cambridge, U. K.

Watts, A. B. (2007), An overview, in *Treatise on Geophysics*, vol. 6, *Crustal and Lithosphere Dynamics*, edited by G. Schubert, pp. 1–48, Elsevier, Amsterdam.